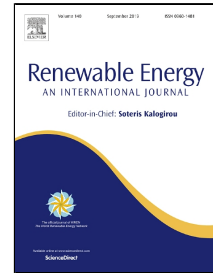


# Accepted Manuscript

Parametric analysis of biomass fast pyrolysis in a downer fluidized bed reactor

Yassir Makkawi, Xi Yu, Raffaella Ocone



PII: S0960-1481(19)30750-5  
DOI: 10.1016/j.renene.2019.05.077  
Reference: RENE 11669  
To appear in: *Renewable Energy*  
Received Date: 08 November 2018  
Accepted Date: 17 May 2019

Please cite this article as: Yassir Makkawi, Xi Yu, Raffaella Ocone, Parametric analysis of biomass fast pyrolysis in a downer fluidized bed reactor, *Renewable Energy* (2019), doi: 10.1016/j.renene.2019.05.077

This is a PDF file of an unedited manuscript that has been accepted for publication. As a service to our customers we are providing this early version of the manuscript. The manuscript will undergo copyediting, typesetting, and review of the resulting proof before it is published in its final form. Please note that during the production process errors may be discovered which could affect the content, and all legal disclaimers that apply to the journal pertain.

# 1 Parametric analysis of biomass fast pyrolysis in a downer fluidized bed 2 reactor

3 Yassir Makkawi<sup>1,\*</sup>, Xi Yu<sup>2</sup>, Raffaella Ocone<sup>3</sup>,

4  
5 *1. Department of Chemical Engineering, American University of Sharjah, P.O. Box 26666,*  
6 *Sharjah, United Arab Emirates*

7 *2. European Bioenergy Research Institute (EBRI), School of Engineering and Applied Science,*  
8 *Aston University, Birmingham B4 7ET, United Kingdom*

9 *3. School of Engineering and Physical Sciences, Heriot-Watt University, Edinburgh EH14 4AS,*  
10 *United Kingdom*

## 11 12 **Abstract**

13 This study presents a theoretical parametric analysis of biomass fast pyrolysis in a downer  
14 reactor, as part of a dual fluidized bed system. The model framework uses a Eulerian-Eulerian  
15 CFD approach and incorporates a user-defined function (UDF) for the thermochemical  
16 conversion of biomass. The downer reactor consists of a novel gas-solid separator, which is  
17 employed to control the gas residence time within the reactor. The parameters investigated  
18 included the reactor temperature, the particles (heat carrier and biomass) and the gas residence  
19 time. The product yield was found to be strongly dependent on the reactor temperature (varied  
20 through changing the heat carrier flow rate), intermediately dependent on the sweeping gas  
21 (N<sub>2</sub>) flow rate and the sand particle size, and much less dependent on the biomass particle  
22 diameter (within the range of 1 mm). The developed model and the results demonstrate the  
23 advantage and robustness of employing the model for parameters optimization and sensitivity  
24 investigation when dealing with complex multiphase flow reactive system. This conclusion  
25 will benefit future development and scale-up studies of downer reactors for biomass fast  
26 pyrolysis.

27  
28 **Keywords:** Biomass, fast pyrolysis, Eulerian-Eulerian, CFD, downer reactor, parametric  
29 analysis.

---

\* Corresponding author: Tel.: +97165152167; fax: +97165152979; E-mail address: [ymakkawi@aus.edu](mailto:ymakkawi@aus.edu) (Yassir T. Makkawi).

## 30 1. Introduction

31 The application of fast pyrolysis for the production of biofuels from biomass is currently  
32 receiving increasing interest driven by the world growing demand for renewable energies. Fast  
33 pyrolysis is a thermochemical process commonly used for the conversion of biomass to liquid  
34 fuel (bio-oil). In this process, the biomass is first thermally degraded in an oxygen deficient  
35 environment to produce pyrolysis gas and biochar. The bio-oil is then produced following rapid  
36 downstream quenching and cooling of the pyrolysis gas.

37

38 During the past few decades, the increasing interest in biomass thermal conversion  
39 technologies has been matched with considerable progress in reactors design and optimization.  
40 The most widely studied reactors for pyrolysis and general biomass thermal conversion are the  
41 fluidized and fixed bed reactors. Reviews on the operating principles and  
42 advantages/disadvantages of the various types of fast pyrolysis reactors are available in the  
43 literature (e.g. Lede [1], Bridgwater [2]). The focus of this study is on a downer reactor (also  
44 referred to as drop tube, free-fall and concurrent fluidized bed). Theoretical and experimental  
45 studies of biomass pyrolysis in a downer reactor are generally rare. The authors are not aware  
46 of any reported theoretical studies fully devoted to the parametric analysis of this type of reactor,  
47 with the exception of the study by the authors, which was focused on the hydrodynamic aspects  
48 of the reactor (Yu et al. [3]). This is despite its distinct advantages, such as uniformity in gas  
49 and solids flow structure compared to up-flow (circulating and bubbling) and fixed bed reactors  
50 (Zhu et al. [4]). In addition to that, downer reactors are known to be simple in design, easier to  
51 operate and control the gas-solid contact time. The latter is a desirable feature in biomass fast  
52 pyrolysis in order to control the product quality. In a simple description, in a conventional  
53 downer reactor, the biomass undergoes rapid thermal degradation while freely falling inside a  
54 hot chamber. In order to create a positive pressure at the entrance and allow sweeping of the  
55 pyrolysis gas, an inert gas, such as nitrogen, is usually introduced at the top. The produced  
56 biochar and pyrolysis gas are collected at the bottom of the reactor, where the latter is rapidly  
57 cooled to produce bio-oil and non-condensable gas. The pyrolysis downer reactor can be  
58 operated in a single mode or integrated within a closed loop to create what is usually referred  
59 to as twin or dual circulating fluidized bed (DCFB) system (see the illustrative diagrams in Fig.  
60 1). In the former case, combustion of a primary biomass feed is used to satisfy the endothermic  
61 pyrolysis reaction of a secondary biomass feed, while in the latter case the process is sustained  
62 by heat supplied from the combustion of the by-product biochar in a second reactor. In this  
63 study, the focus is on the downer pyrolysis reactor as part of a DCFB in Fig. 1-b.

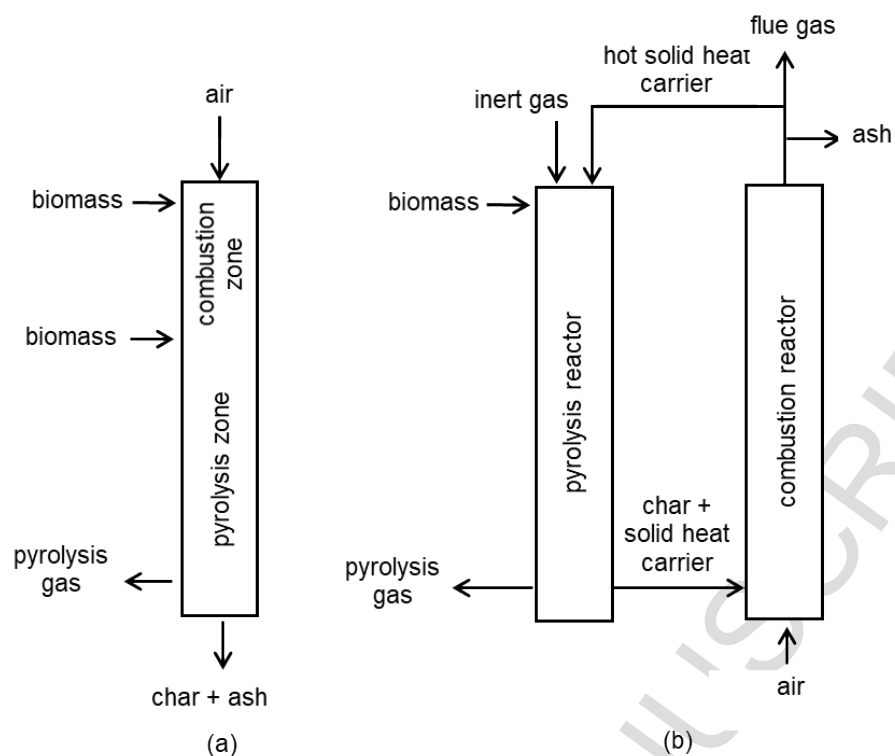


Fig. 1. Examples of the configuration of sustainable biomass pyrolysis reactors without the reliance on external heating (a) single mode fluidized bed (b) twin or dual circulating fluidized bed (DCFB) system.

In pyrolysis experiments, measurement of the process response to the variations of the operating conditions is usually challenging due to the limitation imposed by the nature of the process, i.e. high temperature and release of hydrocarbon gases. Computational fluid dynamic (CFD) offers the option for conducting comprehensive parametric analysis at a low cost with the added advantages of providing detailed localized data (e.g. flow hydrodynamics, temperature and chemical reactions) at a wide range of operating parameters. The use of CFD in the analysis of reactive and non-reactive multiphase flow system has been recently reported in a number of recent publications (e.g. Bashir et al.[5], Elewuwa and Makkawi, [6], Yu et al. [7], Hassan and Makkawi [8]). Of direct relevance to this study is the series of papers by Yu et al. [3, 7] in which a Eulerian–Eulerian CFD model was developed and validated for the prediction of biomass pyrolysis in a downer pyrolysis reactor. The model proved to be highly useful in predicting the details of the flow hydrodynamics and thermochemical behavior in fluidized bed reactors.

97 In biomass pyrolysis, the reaction temperature and the gas residence time are the two most  
98 important parameters to control during the process. Both parameters have been widely reported  
99 to dictate the distribution of the final product (biochar, bio-oil and permanent gas) (Bridgwater  
100 [2], Bridgwater [9]). It is therefore important when designing and operating a pyrolysis reactor,  
101 to keep in mind the relation between the desired quantity/quality of the products and the reactor  
102 operating temperature and gas residence time. The reactor operating temperature is commonly  
103 reported in the parametric analysis of biomass pyrolysis. Its effect is interrelated with other  
104 process parameters, such as the gas residence time and the rate of heat transfer between the gas  
105 and solid phases inside the reactor. For the same type of reactor, the difference in optimum  
106 pyrolysis temperature is mainly due to the variations in the biomass content of lignin, cellulose,  
107 and hemicellulose. Each of these key constituents of biomass decomposes at a different range  
108 of temperature (Lin et al. [10]). The majority of studies have shown a maximum bio-oil yield  
109 at an optimum pyrolysis temperature within the range of 400–900 °C. Bridgwater [9] Suggested  
110 a reaction temperature of around 500 °C is ideal for maximizing bio-oil yield. In an  
111 experimental study by Yu et al. [11], the bio-oil produced from birch wood pyrolysis in a free  
112 fall reactor was found to be maximum at the temperature of 700 °C. In another experiment,  
113 investigating the pyrolysis of pine wood in a bubbling fluidized bed, Westerhof et al. [12] have  
114 shown that the pyrolysis gas yield increases steadily with increasing temperature from 450 to  
115 580 °C then decreases beyond that.

116  
117 The effect of gas residence time is frequently investigated by changing the flow rate of the  
118 sweeping or carrier gas (e.g. Gerçel [13], Gabel [14], Ellens [15]). The sweeping gas  
119 (commonly nitrogen) is used to create an oxygen free environment and control the residence  
120 time of the pyrolysis gas inside the hot zone of the reactor, as noted earlier. Additionally, in  
121 fluidized bed reactors, the sweeping gas serves as a fluidizing medium to promote mixing and  
122 enhances the heat and mass transfer. The sweeping gas flow rate has also a strong effect on the  
123 particle/gas residence time, rate of heating and general flow structure. The gas residence time  
124 can be controlled by increasing or decreasing the sweeping gas flow rate. Short residence time  
125 help in limiting the gas thermal and catalytic cracking during gas-char contact, hence,  
126 increasing the bio-oil yield. In one of the very few studies on experimental parametric analysis  
127 of a free fall reactor, Ellens [15] recommended to maintaining the sweeping gas flow rate in  
128 order to achieve adequate pyrolysis. Gable [14] showed a slightly positive impact of increasing  
129 sweeping gas on the pyrolysis yield. A similar conclusion was reached by Onay and Koçkar

130 [16] who observed that little gain in the bio-oil yields was achieved in a free fall pyrolysis  
131 reactor when increasing the sweep gas flow rates beyond 50 mL/min.

132

133 Other parameters that have been reported to affect the pyrolysis products and the overall reactor  
134 performance are the biomass and heat carrier (sand) particle sizes (e.g. Shen et al. [17], Liu et  
135 al. [18]). Biomass generally has a low thermal conductivity; therefore, it is important to use a  
136 finely ground biomass in order to limit the particle internal thermal resistance (Bridgwater [2]).  
137 Uzun et al. [19] experimentally investigated the effect of the biomass particle size on the bio-  
138 oil yield using a fixed bed reactor at a pyrolysis temperature of 500 C. It was shown that the  
139 optimum biomass particle size for maximum bio-oil yield is within the range of  $0.425 \text{ mm} < d_p$   
140  $< 0.85 \text{ mm}$ . Within this range, negligible variation in the overall process yield and product  
141 distribution was observed. In agreement with this, Jahirul et al. [20] suggested using biomass  
142 particle size  $< 1 \text{ mm}$ . For a biomass particle within this size range and undergoing pyrolysis at  
143 the temperature range of 500 °C the estimated Biot number falls below unity. It is for this reason  
144 that the heat transfer mechanism and release of volatiles at the single particle level remains  
145 independent of the biomass and of the heat carrier particle size as long as the  $d_p$  falls below 1.0  
146 mm. Nevertheless, one should not ignore the important role that particle size plays in  
147 identifying the overall hydrodynamics, such as the solid distribution and the solid velocity.

148

## 149 **2. Process description and objectives of the study**

150 The pyrolysis reactor and the simulation domain considered in this study are shown in Fig. 2.  
151 In this arrangement, the biomass and sand enter the reactor from the top and concurrently flow  
152 towards the bottom under the influence of gravity and drag force exerted by the carrier gas  
153 nitrogen. The sand, which enters at the reactor at a high temperature, is assumed to drive the  
154 endothermic pyrolysis process. At the bottom of the reactor, sand and char are collected in a  
155 receiving tank while the gas is discharged through a pipe inserted under a solid-gas separator.  
156 This separation mechanism, which is specifically designed for downer pyrolysis reactors by  
157 researchers at the ICFAR in Canada [21], has been experimentally tested and numerically  
158 studied by Yu et a. [7] and Huard et al. [22].

159

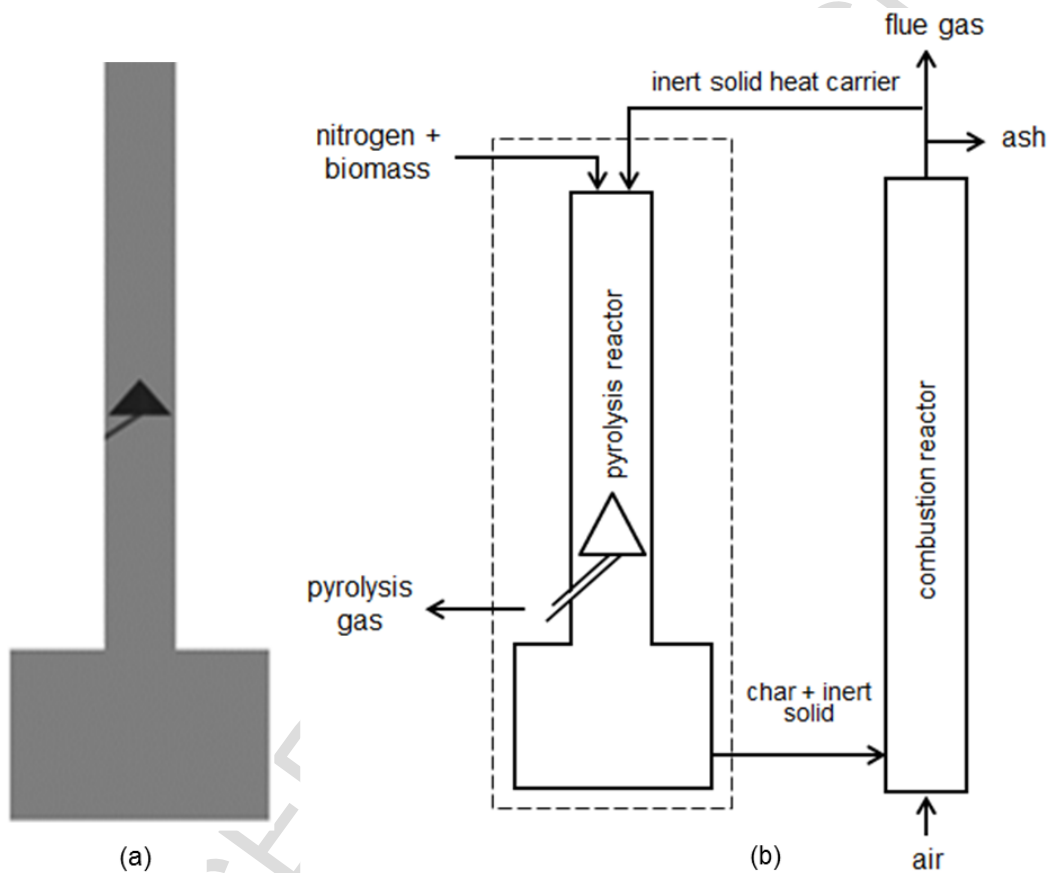
160 The focus of the present parametric study is to elucidate the thermochemical behavior of the  
161 process and the impact of the process parameters on the pyrolysis product yield and distribution.  
162 The specific objectives are:

163 1. To examine the reactor sensitivity and impact of the following parameters on the pyrolysis

164 product yield and overall reactor performance:

- 165 i. Reactor temperature varied through manipulating the flow rate of the heat carrier  
 166 material (sand).  
 167 ii. Gas residence time varied through manipulating the flow rate of the carrier gas  
 168 (nitrogen).  
 169 iii. Biomass and heat carrier (sand) varied through manipulating the particle sizes.  
 170 2. To demonstrate the advantage and robustness of the developed CFD model for the  
 171 parametric analysis of pyrolysis reactors.

172



173

174 Fig. 2. Schematic representation of (a) the pyrolysis reactor simulation domain, and (b) the  
 175 overall closed loop pyrolysis process with the simulation domain inside the dotted box.

176

### 177 3. Model equations

178 The Eulerian-Eulerian CFD model reported by Yu et al. [3, 7] for the simulation of biomass  
 179 pyrolysis in a downer reactor has been used to carry out this parametric analysis. The model is  
 180 solved in three-dimensional coordinates using ANSYS-FLUENT CFD code. The multiphase  
 181 flow inside the reactor is assumed to consist of two solid phases (sand and biomass) and one

182 gas phase consisting of various species, namely, a condensable fraction (bio-oil) and a non-  
 183 condensable fraction consisting of CO, CO<sub>2</sub>, CH<sub>4</sub>, H<sub>2</sub> and H<sub>2</sub>O. The main equations describing  
 184 the hydrodynamics, heat transfer and reaction are given below. The full model, including  
 185 detailed constitutive relations and a user-defined function (UDF) for the pyrolysis reaction, can  
 186 be found in Yu et al. [3, 7].

187

### 188 **3.1. Continuity, momentum and granular energy equations**

189 The gas and solids phases continuity equation are given by:

$$190 \frac{\partial(\alpha_g \rho_g)}{\partial t} + \nabla(\alpha_g \rho_g \bar{u}_g) = R_g \quad (1)$$

$$191 \frac{\partial(\alpha_{s_i} \rho_{s_i})}{\partial t} + \nabla(\alpha_{s_i} \rho_{s_i} \bar{u}_{s_i}) = R_{s_i} \quad i=1 \text{ or } 2 \quad (2)$$

$$192 \sum_{i=1}^2 \alpha_{s_i} + \alpha_g = 1 \quad (3)$$

193 where  $\alpha$  is the volume fraction,  $\rho$  is the density.  $\bar{u}$  is the velocity vector,  $R$  is the interphase  
 194 mass transfer due to biomass pyrolysis and drying. The subscript  $g$ ,  $s_1$  and  $s_2$  stand for gas,  
 195 sand and biomass phases respectively. Note that,  $R_{s_1} = 0$  for the inert solid (sand).

196

197 The gas and solids momentum equations are given by:

$$198 \frac{\partial(\alpha_g \rho_g \bar{u}_g)}{\partial t} + \nabla(\alpha_g \rho_g \bar{u}_g \bar{u}_g) = -\alpha_g \nabla P + \nabla \bar{\tau}_g$$

$$- \sum_{i=1}^2 \beta_{gs_i} (\bar{u}_g - \bar{u}_{s_i}) + \alpha_g \rho_g \bar{g} + \bar{R}_{s_2g} + \dot{m}_{s_2g} \bar{u}_{s_2g}$$

$$199 \quad (4)$$

$$200 \frac{\partial(\alpha_{s_1} \rho_{s_1} \bar{u}_{s_1})}{\partial t} + \nabla(\alpha_{s_1} \rho_{s_1} \bar{u}_{s_1} \bar{u}_{s_1})$$

$$= -\alpha_{s_1} \nabla P - \nabla P_{s_1} + \nabla \bar{\tau}_{s_1} + \beta_{gs_1} (\bar{u}_g - \bar{u}_{s_1}) + \beta_{s_1 s_2} (\bar{u}_{s_2} - \bar{u}_{s_1}) + \alpha_{s_1} \rho_{s_1} \bar{g}$$

$$201 \quad (5)$$

$$202 \frac{\partial(\alpha_{s_2} \rho_{s_2} \bar{u}_{s_2})}{\partial t} + \nabla(\alpha_{s_2} \rho_{s_2} \bar{u}_{s_2} \bar{u}_{s_2})$$

$$203 = -\alpha_{s_2} \nabla P - \nabla P_{s_2} + \nabla \bar{\tau}_{s_2} + \beta_{gs_2} (\bar{u}_g - \bar{u}_{s_2}) + \beta_{s_2 s_1} (\bar{u}_{s_1} - \bar{u}_{s_2}) + \alpha_{s_2} \rho_{s_2} \bar{g} + \bar{R}_{gs_2} - \dot{m}_{s_2g} \bar{u}_{s_2g}$$

$$204 \quad (6)$$

205 where  $\beta_{gs}$  and  $\beta_{ss}$  are the gas-solid and solid-solid momentum exchange coefficients,  
 206 respectively,  $\bar{g}$  is the gravity constant,  $\bar{\tau}$  is the solid shear stress tensor,  $\bar{R}$  is the interphase  
 207 momentum transfer due to the pyrolysis reaction, and  $\dot{m}\bar{u}$  is the interphase momentum transfer



208 due to evaporation. Note that  $\bar{R}$  and  $m\bar{u}$  are not included in Eq. 5, due to the inert nature of the  
 209 sand particles.

210

211 The granular energy equation is given by:

$$212 \quad \frac{3}{2} \left[ \frac{\partial(\alpha_{s_i} \rho_s \theta_{s_i})}{\partial t} + \nabla(\alpha_{s_i} \rho_s \theta_{s_i}) \bar{u}_{s_i} \right] =$$

$$213 \quad (-P_{s_i} \bar{I} + \bar{\tau}_{s_i}) : \nabla \bar{u}_{s_i} + \nabla(\kappa_{\theta_{s_i}} \nabla \theta_{s_i}) - \gamma_{\theta_{s_i}} + \sum_{k=1}^2 \phi_{ks_i} \quad (7)$$

214 where  $\theta_s$  is the pseud-granular temperature of solid phase,  $\kappa_{\theta_s}$  is diffusion coefficient of  
 215 granular energy, and  $\phi_{ks}$  is energy exchange between phase k and solid phase.

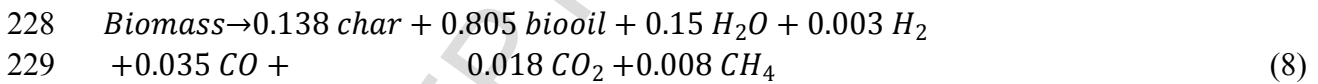
216

217 Note that, in modeling the solid phases it is assumed that the particles are spherical and the  
 218 biomass particle retains its original size during pyrolysis (i.e. no shrinkage). This simplification  
 219 is made due to the recognized shortcomings of the classic Eulerian-Eulerian method which  
 220 lacks the reliable formulation to incorporate the particle shrinkage associated with particle  
 221 drying and pyrolysis.

222

### 223 **3.2. Pyrolysis reaction and drying models**

224 The biomass is treated as a solid phase consisting of volatile matters, fixed carbon, ash and  
 225 water. The composition of the biomass, which is assumed to match that of a switchgrass, is  
 226 given in Table 1. The pyrolysis is described by one-global reaction scheme as follow (Boateng  
 227 and Mtui [23], Yu et al. [7], Bashir et al. [5]):



230

231 According to Eq. (8) the overall non-condensable gas (NCG) is assumed to consist of H<sub>2</sub>, CO,  
 232 CO<sub>2</sub> and CH<sub>4</sub>, with the distribution as per the given coefficients. The rate of the pyrolysis  
 233 reaction is given by the following formula, specifically derived for switch grass pyrolysis as  
 234 follows (Pasangulapati [24]):

$$235 \quad r = \left[ 2.16 \times 10^7 \exp\left(\frac{-1.037 \times 10^7}{RT}\right) \right] \alpha_{s_2} [C_{vol}]^{0.67} \quad (9)$$

236

237 Note that in the above model the homogeneous reactions (between the pyrolysis gas species)  
 238 and heterogeneous catalytic reactions between the gas and char are ignored. This is a reasonable

239 assumption since the employed gas-solid separation mechanism allows for limiting the contact  
 240 between the pyrolysis gas and char while maintaining the gas residence time at the desired  
 241 range of  $< 2$  s (Yu et al. [7]).

242

Table 1. Chemical composition of switch grass (Boateng et al. [25])

	Fixed carbon	Moisture	Volatile	Ash
Proximate analysis (wt%)	13.81	2.65	81.20	2.54
	C	H	O	N
Ultimate analysis (wt%)	48.8	6.99	43.68	0.53

243

244 The biomass drying was incorporated in the model based on evaporative mass transfer process  
 245 where the biomass water content is assumed to be converted to moisture and added to the gas  
 246 phase according to the following mass transfer relation (ANSYS Fluent documentation [26]):

$$247 \quad \dot{m}_{lv} = k_m \times \alpha_l \rho_l \frac{(T_l - T_{sat})}{T_{sat}} \quad (10)$$

248 where  $\dot{m}_{lv}$  is the mass transfer rate from the liquid phase to the vapour phase per unit volume,  $k_m$   
 249  $= 0.1 \text{ s}^{-1}$  is the mass transfer coefficient,  $\alpha_l$  and  $\rho_l$  represent the moisture volume fraction  
 250 and density, respectively,  $T_l$  is the gaseous phase temperature and  $T_{sat}$  is the saturation  
 251 temperature taken as  $100 \text{ }^\circ\text{C}$ .

252

### 253 3.3. Heat balance

254 The heat balance equation for the gas and solid phases are given by:

$$255 \quad \frac{\partial(\alpha_g \rho_g h_g)}{\partial t} + \nabla(\alpha_g \rho_g \vec{u}_g h_g) = \alpha_g \frac{\partial P_g}{\partial t} + \bar{\tau}_g : \nabla \vec{u}_g - \vec{q}_g + S_g + Q_{gs_1} + Q_{gs_2} \\ + (\dot{m}_{s_2g} h_{s_2g} - \dot{m}_{gs_2} h_{gs_2}) \quad (11)$$

$$257 \quad \frac{\partial(\alpha_{s_1} \rho_{s_1} h_{s_1})}{\partial t} + \nabla(\alpha_{s_1} \rho_{s_1} \vec{u}_{s_1} h_{s_1}) = \alpha_{s_1} \frac{\partial P_{s_1}}{\partial t} + \bar{\tau}_{s_1} : \nabla \vec{u}_{s_1} - \vec{q}_{s_1} + Q_{s_1g} \quad (12)$$

$$258 \quad \frac{\partial(\alpha_{s_2} \rho_{s_2} h_{s_2})}{\partial t} + \nabla(\alpha_{s_2} \rho_{s_2} \vec{u}_{s_2} h_{s_2}) = \alpha_{s_2} \frac{\partial P_{s_2}}{\partial t} + \bar{\tau}_{s_2} : \nabla \vec{u}_{s_2} - \vec{q}_{s_2} - S_g + Q_{s_2g} \\ + (\dot{m}_{gs_2} h_{gs_2} - \dot{m}_{s_2g} h_{s_2g}) \quad (13)$$

259 where  $h_g$  is the specific enthalpy of the gas phase,  $\vec{q}$  is the heat flux,  $S$  is a source term that  
 260 includes the enthalpy due to the chemical reaction,  $Q$  is the intensity of the heat exchange  
 261 between the gas and solid phases. The last term on the right-hand side represents the interphase  
 262

263 enthalpy exchange due to evaporation. Note that, in the above heat balance, the internal thermal  
 264 resistance at the single particle level is neglected due to the low Biot numbers for both the solid  
 265 phases (sand and biomass particles).

266

#### 267 4. Model solution procedure and boundary conditions

268 The model equations are solved using finite volume approach. First-order discretization  
 269 schemes were used for the solution of the convection terms in all governing equations. The  
 270 relative error between any two successive iterations was specified by using a convergence  
 271 criterion of  $10^{-3}$  for each scaled residual component. The phase-coupled SIMPLE algorithm  
 272 (Vasquez and Ivanov [27]) was applied for the pressure-velocity coupling. The linearized  
 273 governing equations were solved using the block algebraic multi-grid method. In order to avoid  
 274 numerical instabilities and to ensure that the fast biomass conversion and heat transfer are  
 275 captured, the solution time step for the reactive system was set to a relatively smaller time step  
 276 of 0.0005 s for the first 0.5 s then increased to 0.001 s for the rest of the simulation time. The  
 277 mesh was generated with hybrid cells of structured and unstructured grids, giving a total of  
 278 30,785 cells. In order to capture the steep hydrodynamic variations around the walls of the  
 279 separation device (the conical deflector and the gas exit pipe), the grid size was refined by  
 280 setting the minimum and maximum grid size at 0.3 and 1.0 cm, respectively. In the remaining  
 281 of the simulation domain, the minimum and maximum grid size were set at 1.0 and 5.0 cm.  
 282 respectively. Summary of the reactor dimensions, default operating conditions and simulation  
 283 parameters are given in Table 2.

284

285 Table 2. Summary of the reactor dimensions and the defaults operating conditions

<b>Reactor dimensions*</b>			
Reactor height [m]	1.335	Diameter of the gas exit pipe [cm]	0.95
Reactor diameter [m]	0.069	Position of gas exit from top [cm]	98.6
<b>Default operating parameters</b>			
Pressure outlet [pa]	101,3	Biomass inlet temperature [°C]	25.0
Biomass flow rate [g/s]	5.0	N <sub>2</sub> inlet temperature [°C]	25.0
Nitrogen flow rate [lit/s]	0.187	Sand inlet temperature [°C]	700.0
Sand flow rate [g s <sup>-1</sup> ]	80.0	Sand particle size [mμ]	200.0
Sand density [kg m <sup>-3</sup> ]	2650	Biomass particle size [mμ]	500
<b>Simulation parameters</b>			
Wall-particle restitution coef. [-]	0.8	Maximum solid packing [-]	0.63
Particle-particle restitution coef. [-]	0.9	Specularity coefficient [-]	0.5

Solution convergence criterion (-)	10 <sup>-3</sup>	Maximum number of iterations [-]	20
------------------------------------	------------------	----------------------------------	----

286 \* Further details on the reactor and separator geometry are available in Yu et al. 2014 [3]  
287

288 Table 3. shows the summary of the parameters varied in this study, taking into consideration  
289 the effect of the heat carrier (sand) flow rate, particles sizes (sand and biomass) and sweeping  
290 gas (nitrogen) flow rate on the pyrolysis products distribution. In total, this makes nine different  
291 simulation conditions, including the default setting of Case No 1.

292

293 Table 3. Set of the operating conditions considered in the parametric analysis

Parameter	Default	Parameters varied							
		N <sub>2</sub> flow		Sand flow		Particle size			
						Biomass		Sand	
Case No	1	2	3	4	5	6	7	8	9
N <sub>2</sub> flow rate [m <sup>3</sup> /h]	0.67	<b>0.34</b>	<b>6.73</b>	0.67	0.67	0.67	0.67	0.67	0.67
Sand flow [g/s]	80	80	80	<b>50</b>	<b>100</b>	80	80	80	80
Biomass size [μm]	500	500	500	500	500	<b>200</b>	<b>350</b>	500	500
Sand size [μm]	200	200	200	200	200	200	200	<b>350</b>	<b>500</b>

294

## 295 5. Parametric analysis and discussion

### 296 5.1. Effect of the reactor temperature

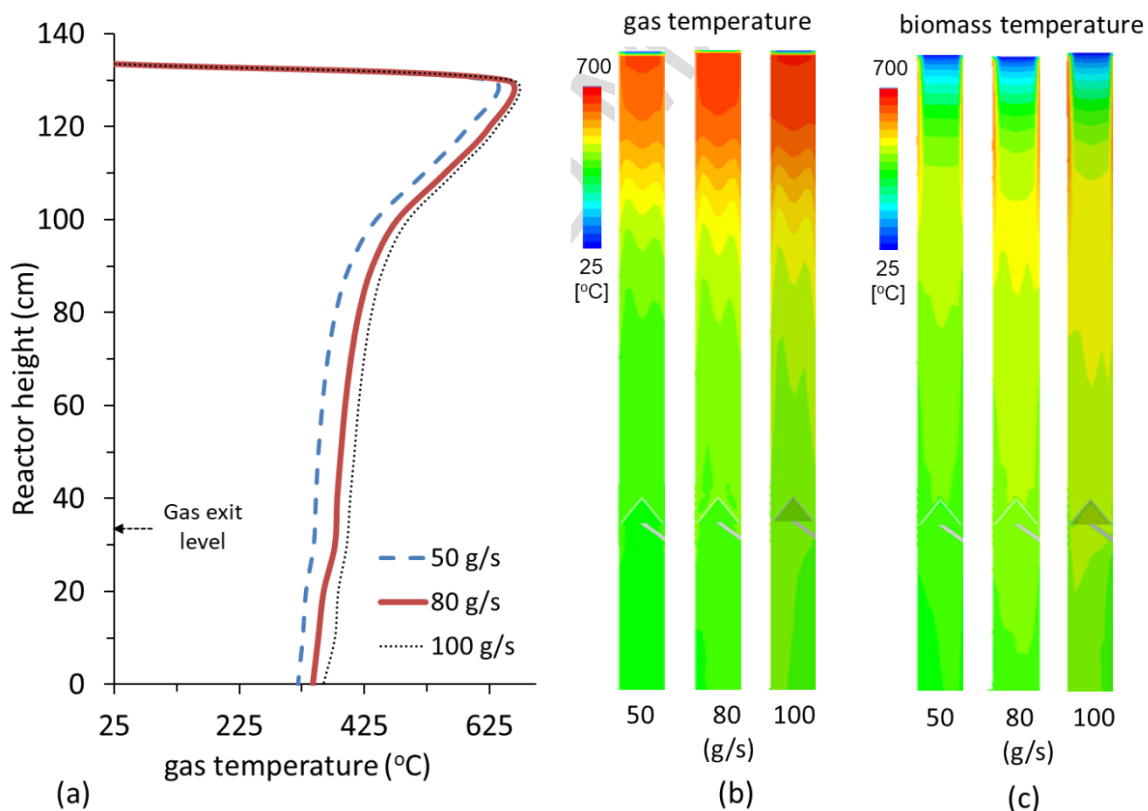
297 The reactor temperature was varied by varying the heat carrier (sand) flow rate. The choice is  
298 made here to vary the sand flow rate because this resembles largely the effects caused by  
299 varying the sand temperature with the added advantage of providing the necessary data to  
300 assess the associated change in flow hydrodynamics. The range of sand flow rate considered  
301 in the analysis was selected based on the following simple energy balance equation:

$$302 \quad Q_{in} = \sum m \Delta H_{f,298,feed}^{\circ} + \sum m \Delta H_{feed}(T) - \sum n \Delta H_{f,298,prod}^{\circ} - \sum n \Delta H_{prod}(T) \quad (14)$$

303 where  $\Delta H_{f,298,feed}^{\circ}$  and  $\Delta H_{f,298,prod}^{\circ}$  are the heats of formation of feed and product materials at  
304 temperature 298K per kg material;  $H_{feed}(T)$  and  $H_{prod}(T)$  are the enthalpies of the feed and  
305 products at temperature  $T$  (pyrolysis temperature). Using the above equation, the estimated heat  
306 input required to derive the pyrolysis of 5 g/s biomass flow is 9.3 KW. For sand entering at  
307 700 °C and assuming an average reactor temperature of 500 °C, this heat corresponds to sand  
308 flow of around 80 g/s. Therefore, to assess the sensitivity of the downer reactor to the operating  
309 temperature, three different sand flow rates of 50, 80 and 100 g/s has been considered. Note  
310 that this corresponds to 10–20 times the biomass feed rate, which is within the rule of thumb  
311 for thermal conversion of biomass in fluidized bed reactors.

312

313 Fig. 3 shows the profiles and contours of the biomass phase temperature at three different sand  
 314 flow rates of 50 g/s, 80 g/s and 100 g/s. As expected, the increase in the heat carrier flow rate  
 315 has a direct impact on the reactor temperature, as well as on the overall flow hydrodynamics.  
 316 In Fig. 3a,b, the profile and contour show that the gas temperature increases sharply from 25 °C  
 317 to above 600 °C within a very short entrance length due to the rapid heat transfer from the hot  
 318 sand (heat carrier) to the gas and biomass phases. The temperature then gradually decrease but  
 319 with a much lesser extent beyond the lower part of the reactor. The drop in the gas temperature  
 320 is due to the heat being consumed by drying and pyrolysis of the biomass. The contours of the  
 321 biomass temperature, shown in Fig. 3c, depicts a different behavior where it is observed that  
 322 the biomass temperature gradually increases from the entrance temperature of 25 °C to reach a  
 323 peak within the upper part of the reactor. The temperature then remains relatively uniform and  
 324 steady within most of the lower part of the reactor. Generally, it is observed that the “thermal  
 325 entrance length” slightly increases with increasing the heat carrier flow rate, which is expected,  
 326 since this increases the heat supply.  
 327



328  
 329 Fig. 3. Variations in the gas and biomass temperatures at various sand flow rates (50–100 g/s)  
 330 (a) cross-sectional average vertical profile of biomass temperature (b) and (c) contours of the  
 331 biomass and gas temperatures, respectively.

332

333 Fig 4 shows the vertical profile of devolatilization efficiency and contours of the  
 334 devolatilization rate at the three different sand flow rates considered. The efficiency was  
 335 calculate cumulatively using the following formula:

$$336 \eta_{dev} = \frac{m_{volatile} \text{ removed from biomass}}{m_{volatile} \text{ in the biomass feed}} \quad (15)$$

337

338 Fig. 4a shows that the cumulative devolatilization efficiency curves consistently shift to the  
 339 right as the sand flow rate is increased from 50 g/s to 100 g/s. In Fig. 4b, it is generally observed  
 340 that the devolatilization rate is nearly zero within the thermal entrance length. This is not  
 341 surprising since this is the region where the biomass and carrier nitrogen undergo rapid  
 342 convective heating by the hot sand. The devolatilization then commences shortly after that, as  
 343 indicated in the contours plots. Beyond the gas exit pipe, the devolatilization rate sharply  
 344 decreases mainly due to the drop in temperature. At this stage, the biomass is converted to the  
 345 final product of pyrolysis gas and char.

346

347

348

349

350

351

352

353

354

355

356

357

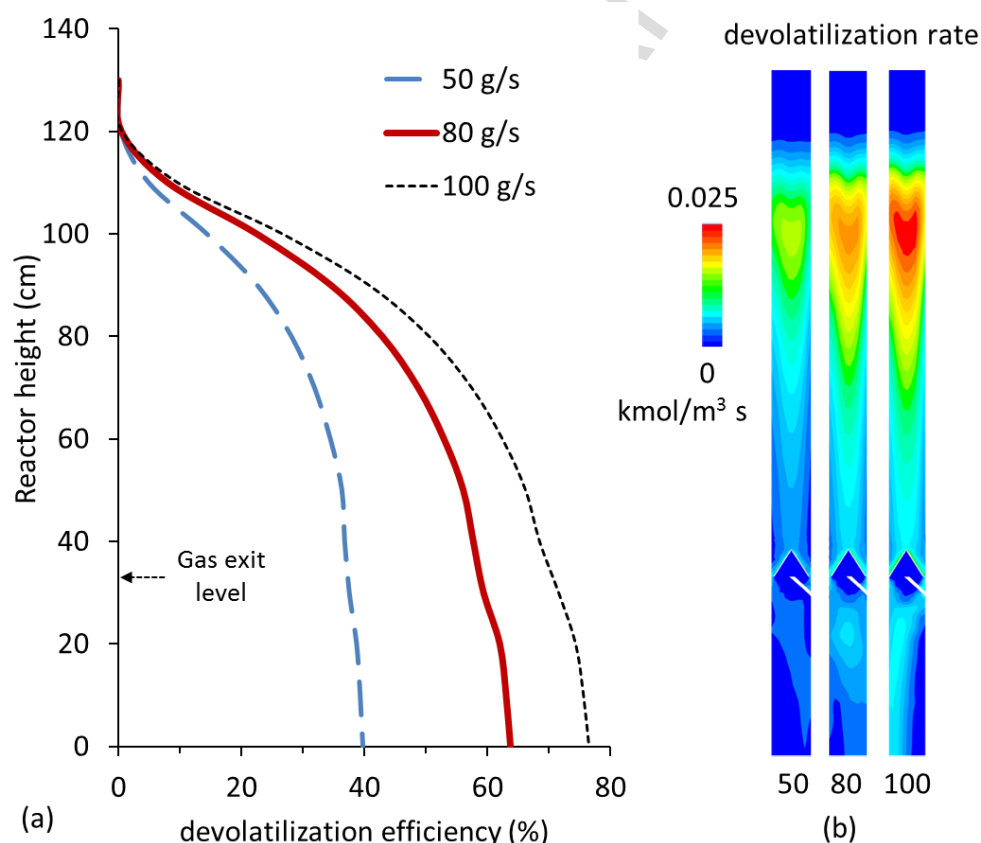
358

359

360

361

362



362

363 Fig. 4. Biomass devolatilization at steady condition for different heat carrier (sand) flow rates  
 364 (a) variations of the devolatilization efficiency along the reactor height (b) contours of  
 365 devolatilization rate.

366

367 Fig. 5 shows the temporal evolution of the pyrolysis gas flow and the final product distribution  
368 at different sand flow rates. The products consist of liquid bio-oil including water, non-  
369 condensable gas (NCG) and char. Fig. 5a shows that the flow of the pyrolysis gas reaches the  
370 steady state after  $\sim 2$  s from the start of the operation. The results also suggest that the flow of  
371 the pyrolysis gas increases linearly with increasing the sand flow rate. The data in Fig. 5b shows  
372 the bio-oil and NCG to increase with increasing the heat carrier flow, which comes at the  
373 expense of decreasing the char yield. This is in agreement with the vast majority of published  
374 literature (e.g. Demirbas, 2004 [28]), since increasing the reactor temperature tends to convert  
375 the biomass to higher fraction pyrolysis gas with lower biochar production. It should be noted  
376 that excessive increase in the reactor temperature, beyond the critical temperature of  $\sim 600$  °C  
377 shifts the pyrolysis process towards the gasification model as the volatiles get thermally  
378 cracked to light hydrocarbons, while the char is constituted predominantly by ash and fixed  
379 carbon. In the current model, thermal cracking, as well as the reaction between the biochar and  
380 gas, are omitted because the temperature remains within the recommended limit and the gas  
381 residence time within the hot zone of the reactor is short, as demonstrated in the following  
382 section. Quantitatively, the calculation shows that as the temperature is increased by doubling  
383 the sand flow (from 50 to 100 g/s), the bio-oil yield and the NCG both increased by 118% and  
384 124%, respectively, which is significantly high.

385

## 386 **5.2. Effect of biomass and sand particle sizes**

387 The reaction rate in pyrolysis is widely understood to be strongly dominated by the heat transfer  
388 at the particle level. However, the current Eulerian-Eulerian model treats the solid as a  
389 continuum phase; hence, the internal thermal resistance, at the single particle level is not  
390 incorporated. This is a valid approximation if the particle Biot number is below unity. Here,  
391 the Biot number is calculated as follows:

$$392 \quad Bi = \frac{d_c h}{k} \quad (16)$$

393 where  $d_c$  is a characteristic length [m],  $h$  is the convective heat transfer coefficient [ $\text{W m}^{-2} \text{K}^{-1}$ ]  
394 and  $k$  is the thermal conductivity of the particle [ $\text{W m}^{-1} \text{K}^{-1}$ ]. Assuming an average pyrolysis  
395 temperature of 500 °C, heat transfer coefficient of 0.65  $\text{kW m}^{-2} \text{K}^{-1}$ , and thermal conductivity  
396 of 0.25 and 0.1  $\text{W m}^{-1} \text{K}^{-1}$  for sand and biomass particles respectively, the calculated Biot  
397 number was found to fall below unity, hence the approximation employed is valid, as noted  
398 earlier. There is also experimental evidence, such as that reported by Seebauer et al., (1979)

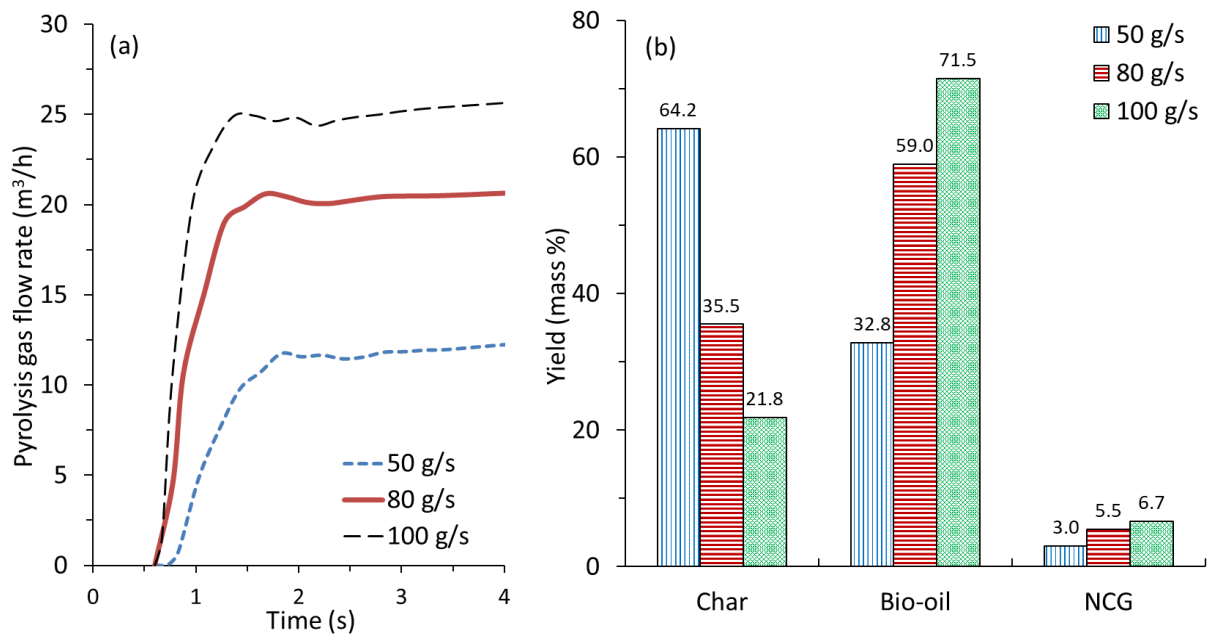
399 [29] and Septien (2012) [30], which indicates that the effect of the particle size on the pyrolysis  
400 yield is negligible as long as the size falls below 1.5 mm. The solid-solid conductive heat  
401 transfer is also ignored in the current model due to the very low solid concentration. This  
402 implies that the change in the particle size would only affect the overall rate of pyrolysis  
403 through changing the flow hydrodynamics and the particle surface area available for heat and  
404 mass transfer.

405  
406 Fig. 6 shows the distribution of the biomass solid phase at three different particle sizes (200,  
407 350 and 500  $\mu\text{m}$ ) and the corresponding pyrolysis product distribution. Note that the colour  
408 code in the contours has been restricted to allow better visualization of the solid concentration  
409 variations. In Fig. 6a, it is generally observed that the biomass concentration is high at the  
410 entrance and to a lesser extent below the gas exit at the separator. It is also clear that the effect  
411 of changing the particle size is limited, consequently, there is a limited impact of this parameter  
412 on product distribution, as shown in Fig 6b. This is expected since the biomass flow rate is too  
413 low to cause a significant impact on the reactor hydrodynamics. On the contrary, the effect of  
414 changing the sand particle size on the flow hydrodynamics and products is well-pronounced,  
415 as shown in Fig. 7. Note that the sand flow rate is at least 10 times higher than that of the  
416 biomass. In Fig. 7a, the overall flow structure appears to be completely re-shaped at increasing  
417 sand flow by forming a highly dense core and dilute walls. This appears to have a positive  
418 impact on the bio-oil and NCG gas yields, as shown in Fig. 7b. The decrease in sand particle  
419 size, from 500  $\mu\text{m}$  to 200  $\mu\text{m}$ , resulted in increasing the bio-oil and the NCG yields by  $\sim 30\%$ ,  
420 at the expense of a decrease in the char yield. This could also be attributed to the fact that,  
421 smaller particles offer higher surface area, hence, higher heat and mass transfer between the  
422 various phases. This, in turn, enhances the overall rate of release of pyrolysis gas.

423  
424  
425  
426  
427  
428  
429  
430  
431  
432



433  
434  
435



436

437 Fig. 5. Effect of the heat carrier flow rate (sand) on the release of pyrolysis gas and product  
438 composition (a) Temporal evolution of the pyrolysis gas flow rate at the gas exit pipe, and (b)  
439 the corresponding product distribution at different sand (heat carrier) flow rates.

440

441

442

443

444

445

446

447

448

449

450

451

452

453

454

455

456

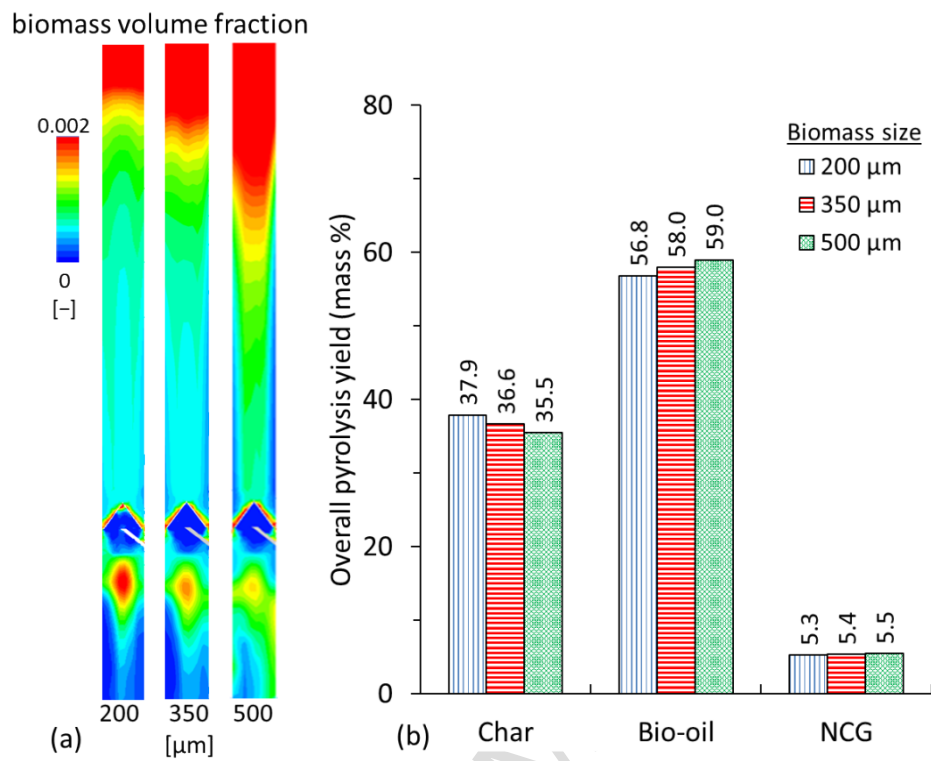
457

458

459

460

461



462 Fig. 6. Effect of the biomass particle size (200–500 μm) on (a) the biomass concentration, and  
 463 (b) the pyrolysis products distribution.

464

465

466

467

468

469

470

471

472

473

474

475

476

477

478

479

480

481

482

483

484

485

486

487

488

489

490

491 Fig. 7. Effect of the sand particle size on (a) the sand concentration, and (b) the pyrolysis  
492 products distribution.

493

494

495

496

497

498

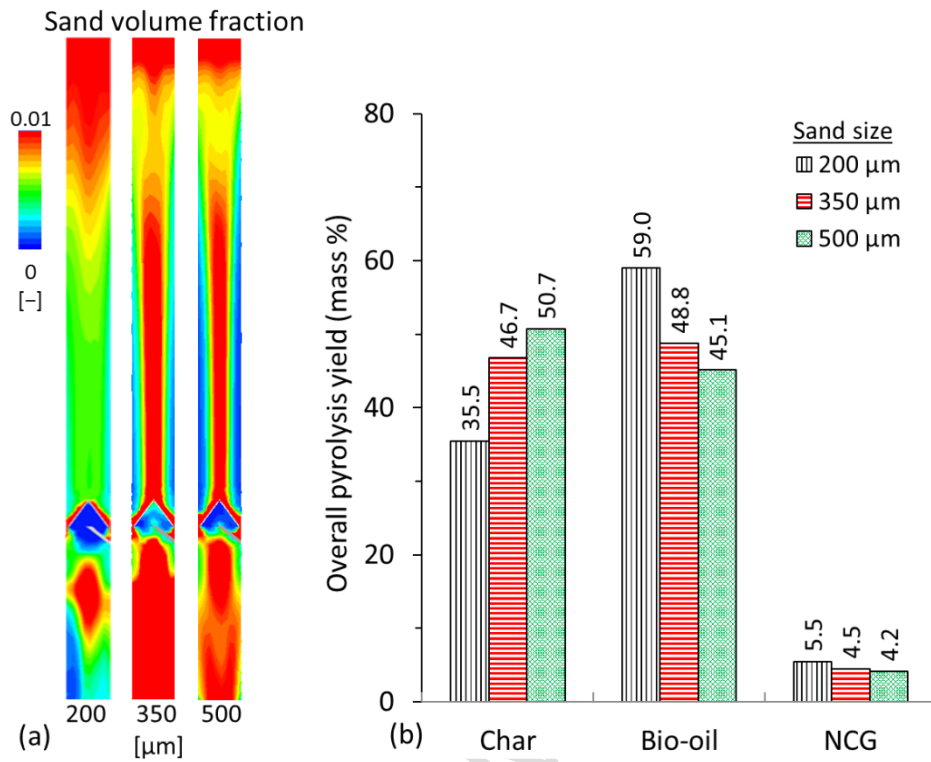
499

500

501

502

503



### 504 5.3. Effect of nitrogen flow rate

505 Inert gases, such as nitrogen, helium and argon, are commonly used in biomass fast pyrolysis  
 506 in order to (i) create an oxygen-free environment (ii) allow sweeping of the produced pyrolysis  
 507 gas, and, most importantly, (iii) control the gas and solid residence time within the hot reaction  
 508 zone. In this study, the effect of nitrogen flow was studied using three different flow rates; two  
 509 within the low flow range (0.34 m<sup>3</sup>/h and 0.67 m<sup>3</sup>/h) and one excessively high (6.73 m<sup>3</sup>/h). The  
 510 flow rates correspond to nitrogen inlet velocities of 0.025 m/s, 0.05 m/s and 0.5 m/s,  
 511 respectively. All the other operating parameters were set at the default values, as given in Table  
 512 2. In order to relate the applied gas flow to the drag force exerted on particles, the following  
 513 force balance for a particle in suspension (Makkawi [31]) has been used:

$$514 F_d = \frac{\pi}{8} d_p^2 \rho_f (u_g)^2 C_d \quad (17)$$

515 where

$$516 C_d = 3.0 + 303e^{-0.135Re_p} \quad (18)$$

517

518 Applying Eqs. 17 and 18 for a biomass particle of 500 μm diameter, the ratio of the gas drag  
 519 force to the particle weight force ( $F_d/W$ ) at the nitrogen velocities of 0.025 m/s, 0.05 m/s and  
 520 0.5 m/s would be 0.07, 0.23 and 3.13, respectively. In the next paragraphs, it is shown that the  
 521 ratio  $F_d/W$  is of significance for the relation between the gas flow rate, gas residence and the  
 522 particle weigh force with the pyrolysis yield.

523

524 Fig. 8 shows the effect of the nitrogen flow rate on the distribution of the gas residence time  
 525 (time taken from the inlet to the gas exit pipe). The residence time distribution was obtained  
 526 based on particle tracking and path lines analysis method [Ghirelli et al. [32]]. It is shown that  
 527 at the highest nitrogen flow rate the gas residence time distribution is narrowed within the range  
 528 of 0.3–1.3 s and peaks at ~0.5 s, while at the lowest nitrogen flow, the residence time is widely  
 529 distributed within the range of 0.5–4 s with a peak at 2 s. In between, at the nitrogen velocity  
 530 of 0.05 m/s, the residence time distribution is within the range of 0.7–2.7 s and peaks at ~1.5  
 531 s, which is close to the range recommended for maximum bio-oil yield by fast pyrolysis (1–2  
 532 s) (Bridgwater and Peacocke [33]).

533

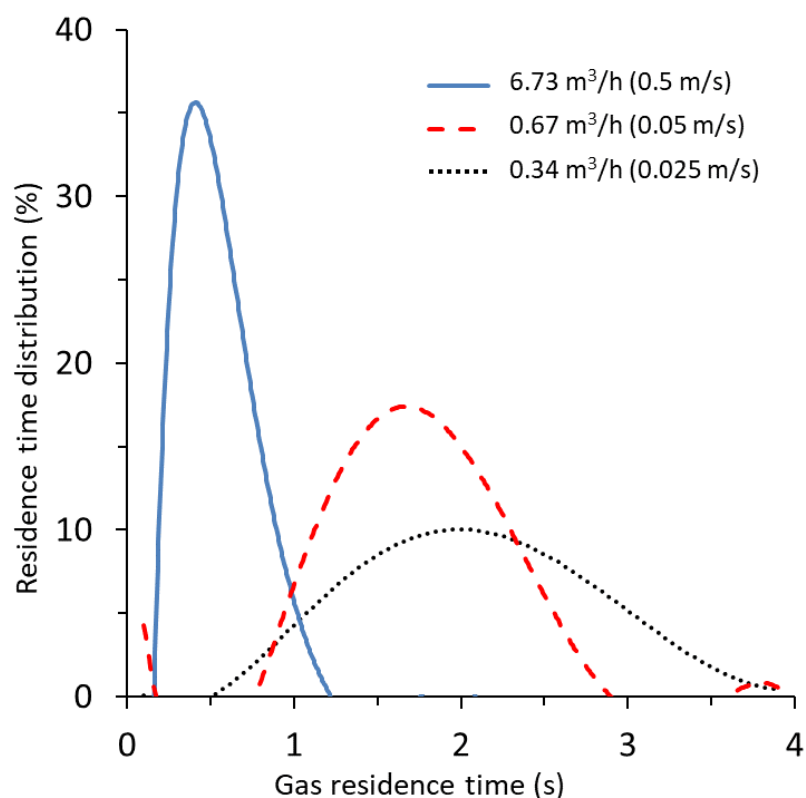
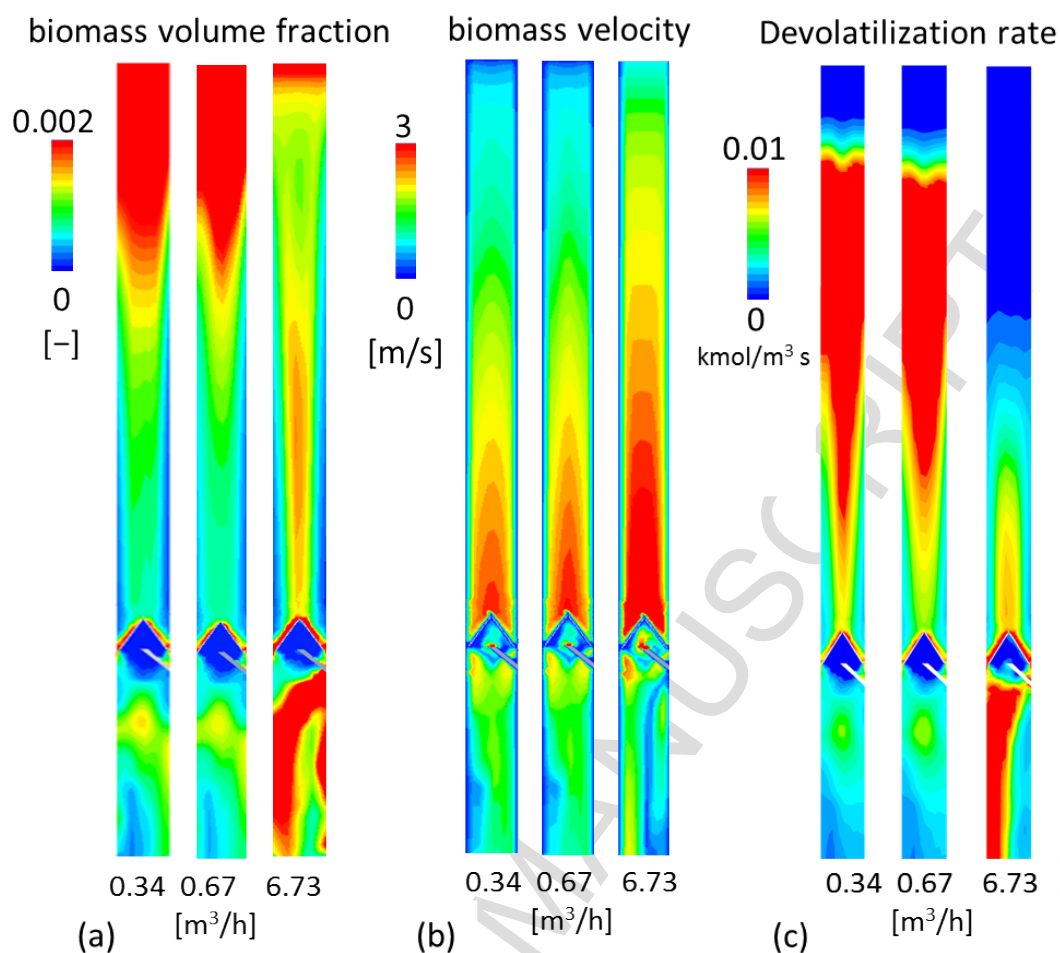


Fig. 8. Effect of the nitrogen flow rate (0.34–6.73 m<sup>3</sup>/h) on the gas residence time.

In addition to affecting the gas residence time, the nitrogen flow rate also plays an important role in defining the biomass distribution (volume fraction), velocity and devolatilization rate, as demonstrated in Fig. 9. A dramatic change in the biomass velocity and concentration takes place when the nitrogen flow rate is increased from 0.673 m<sup>3</sup>/h to 6.73 m<sup>3</sup>/h. Note that, at 6.73 m<sup>3</sup>/h nitrogen flow, the estimated drag force exerted on the biomass is high, more than 3 times higher the particle weight force. At this condition, the biomass is packed below the gas exit pipe (see the third contour in Fig. 9a), while the velocity is excessively high in most of the upper part of the reactor (see the third contour in Fig. 9b). Obviously, this will have a negative impact on the mass and heat transfer rates at the core of the reactor due to the non-uniformity in flow structure. It is also clear from the contour in Fig. 9c that the devolatilization rate is close to zero in most of the upper part of the reactor.

563  
564  
565  
566  
567  
568  
569  
570  
571  
572  
573  
574  
575  
576  
577  
578  
579  
580  
581

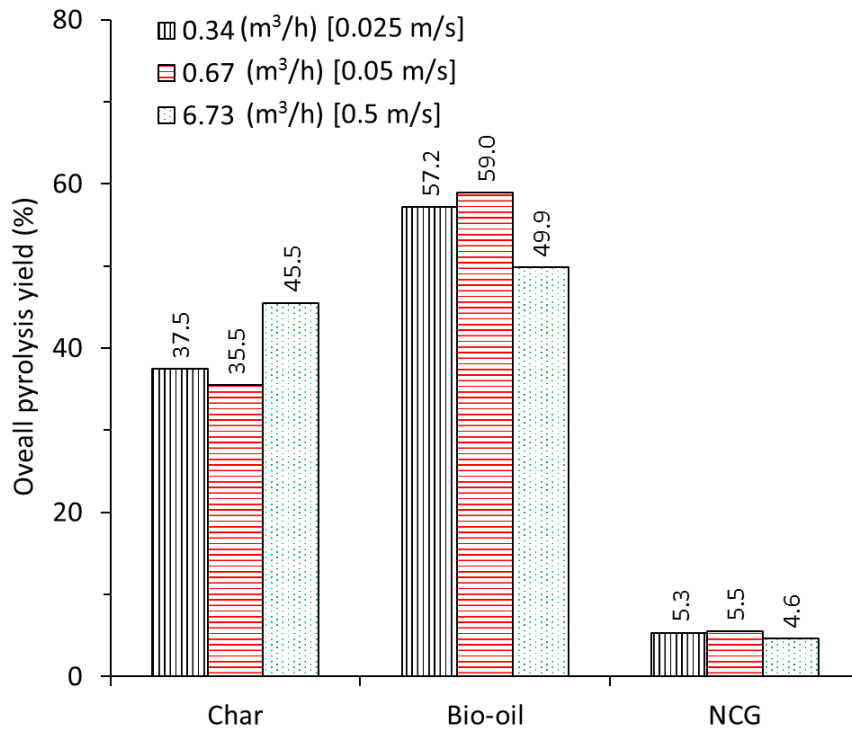


582 Fig. 9. Effect of the nitrogen flow rate (0.34–6.73 m<sup>3</sup>/h) on (a) biomass volume fraction (b)  
583 biomass velocity (the biomass volume fraction is restricted to 0.002 to allow better  
584 visualization) and (c) on biomass devolatilization rate.

585

586 Finally, Fig. 10 shows the effect of nitrogen flow rate on the overall pyrolysis product yield.  
587 Operating at the nitrogen velocity of 0.05 m/s (0.67 m<sup>3</sup> h<sup>-1</sup>) appears to give high bio-oil yield  
588 (59.0 wt%). At the highest nitrogen flow rate of 0.5 m/s (6.73 m<sup>3</sup> h<sup>-1</sup>), the bio-oil and the NCG  
589 drop by 15% and 11%, respectively, which comes at the expense of increasing the char. This  
590 is due to insufficient biomass and gas residence times and the negative impact of this on the  
591 reactor temperature and overall flow hydrodynamics. As noted earlier in the introduction,  
592 various studies on free fall or downer reactors have discussed the optimum sweeping gas flow  
593 or velocity for maximum bio-oil yield (e.g. Gable [14]; Ellens [15]; Onay and Kockar [16]).  
594 However, generalization of such results for different reactors sizes and operating conditions is  
595 meaningless. It is of more relevance to use the relation between the sweeping gas drag force

596 and the particle weight force ( $F_d/W$ ), since this is indirectly indicative of the relation between  
 597 the sweeping gas flow, residence time and heat transfer rate for a particle undergoing pyrolysis  
 598 in a downer reactor. In this study, the maximum bio-oil and NCG yield was found at  $F_d/W =$   
 599 0.23.



616 Fig. 10. Effect of the nitrogen flow rate (0.34–6.73 m³/h) on the distribution of the pyrolysis  
 617 products.

## 619 6. Conclusions

620 Parameter sensitivity analysis of biomass fast pyrolysis in a downer reactor has been studied  
 621 using a Eulerian-Eulerian CFD approach where the pyrolysis is considered to undergo one  
 622 global step reaction. According to the predicted results, the following conclusions are made:

- 623 a) The pyrolysis temperature is the most effective parameter in the overall product yield  
 624 and distribution. In this study, the temperature has been changed by increasing the heat  
 625 carrier flow rate from 50 g/s up to 100 g/s. This has been found to increase considerably  
 626 the bio-oil and NCG yields by 118% and 124%, respectively, at the expense of  
 627 decreasing the bio-char yield.
- 628 b) The change in the biomass particle size within the range of 200–500  $\mu\text{m}$ , has been

629 found to cause a negligible effect on the reactor hydrodynamics and overall product  
630 yield and distribution. The effect of the sand particle size, on the other hand, has been  
631 found to cause a major change in the reactor flow structure as well as in the products  
632 yield. The bio-oil and NCG yields both increased by around 30% when decreasing the  
633 particle size from 500  $\mu\text{m}$  to 200  $\mu\text{m}$ . This is mainly due to the increase in heat transfer  
634 surface area as the particle size decreases.

- 635 c) The nitrogen flow rate strongly affects the gas residence time. Excessive nitrogen flow,  
636 exerting a drag force higher than the single particle weight ( $F_d/W \gg 1.0$ ), may result  
637 in shifting the gas residence time beyond the recommended range for fast pyrolysis  
638 (1–2 s). In this study, operating at a moderate gas flow of 0.67  $\text{m}^3/\text{h}$  (0.05  $\text{m/s}$ ), which  
639 is calculated to correspond to  $F_d/W = 0.23$ , is found to produce the highest bio-oil and  
640 NCG yields. At this condition, the hydrodynamics and devolatilization rate appear to  
641 improve, with the latter rapidly taking place within the upper core section of the reactor.
- 642 d) The investigated parameters are interrelated; therefore, any optimization or  
643 extrapolation of the operating conditions for a targeted product (bio-oil, char or NCG)  
644 must be exercised with caution.

645  
646 **Acknowledgment:** The authors thank The Leverhulme Trust (UK) for a research grant (RPG-  
647 410).

648  
649  
650  
651  
652  
653



**Notations**

$A_i$	Interfacial area (m <sup>2</sup> )
$C_p$	Specific heat (J kg <sup>-1</sup> K <sup>-1</sup> )
$C_{vol}$	Concentration of volatiles in biomass (mol m <sup>-3</sup> )
$d_i$	Diameter of solid phase $i$ (m)
$E$	Activation energy (-)
$\vec{g}$	Gravity (m s <sup>-2</sup> )
$h$	Specific enthalpy (kJ kg <sup>-1</sup> )
$h'$	Heat transfer coefficient (w m <sup>2</sup> k <sup>-1</sup> )
$H(T)$	Enthalpy at temperature T (KJ/kg)
$\Delta H_{f,298}^{\circ}$	Heat of formation at temperature 298K (KJ/kg)
$\vec{J}_{i,g}$	Diffusion flux of species $i$ (kg m <sup>-2</sup> s <sup>-1</sup> )
$k_m$	Mass transfer coefficient (s <sup>-1</sup> )
$L$	Reactor length (m)
$\dot{m}$	Mass transfer rate (kg m <sup>-3</sup> s <sup>-1</sup> )
$Nu_{s_i}$	Nusselt number of solid phase $i$ (-)
$P$	Pressure (pa)
$Pr$	Prandtl number (-)
$\vec{q}$	Heat flux (w m <sup>-3</sup> )
$Q_{gs1}$	Intensity of heat exchange between gas and solid (kJ m <sup>-3</sup> s <sup>-1</sup> )
$Q_{in}$	Required thermal input for pyrolysis (Kw)
$R$	8.314 (J/mol K)
$R_g, R_{s_i}$	Interphase mass transfer term (kg m <sup>-3</sup> s <sup>-1</sup> )
$Re_{s_i}$	Reynolds number of solid phase $i$ (-)
$r$	Rate of pyrolysis reaction (mol m <sup>-3</sup> s <sup>-1</sup> )
$S$	Source of enthalpy due to chemical reaction (kJ m <sup>-3</sup> s <sup>-1</sup> )
$T$	Temperature (K)
$t$	Time (s)
$\vec{u}_g, \vec{u}_{s_i}$	Gas and solid velocity vectors, respectively (m s <sup>-1</sup> )
$U_{mf}$	Minimum fluidization velocity (m s <sup>-1</sup> )
$U_p$	Particle velocity (m s <sup>-1</sup> )
$Y_{i,g}$	Mass fraction

**Greek symbols**

$\alpha_g, \alpha_{s_i}$	Volume fraction of gas and solid phase $i$ respectively (-)
$\beta$	Momentum exchange (drag) coefficient (kg m <sup>-3</sup> s <sup>-1</sup> )
$\gamma_{\theta_{s_i}}$	Collisional energy dissipation (kg m <sup>-1</sup> s <sup>-3</sup> )
$\eta$	Separation efficiency (-)
$\theta_{s_i}$	Granular temperature of solid phase $i$ (m <sup>2</sup> s <sup>-2</sup> )
$\kappa_{\theta_{s_i}}$	Diffusion coefficient of granular energy (kg m <sup>-1</sup> s <sup>-1</sup> )
$\lambda_{s_i}$	Particle bulk viscosity (kg m <sup>-1</sup> s <sup>-1</sup> )
$\rho_g, \rho_{s_i}$	Gas and solid densities, respectively (kg m <sup>-3</sup> )
$\tau$	Solid residence time (s)
$\bar{\tau}$	Shear stress tensor (kg m <sup>-1</sup> s <sup>-2</sup> )

654

655

656 **References**

- 657 [1] Lede, Jacques, Biomass Fast Pyrolysis Reactors: a Review of a few Scientific Challenges and of  
658 Related Recommended Research Topics. Oil & Gas Science and Technology– Rev. IFP Energies  
659 nouvelles, Vol. 68 (2013), No. 5, 801-814.  
660
- 661 [2] A. V. Bridgwater, Review of fast pyrolysis of biomass and product upgrading, Biomass and  
662 Bioenergy, 38 (2012) 68-94.  
663
- 664 [3] Yu, X., Makkawi, Y., Ocone, R., Berruti, F., Beriens, C., Huard, M., A CFD study of biomass  
665 pyrolysis in a downer reactor equipped with a novel gas-solid separator - I: hydrodynamic performance.  
666 Fuel Processing Technology (2014), 366-382.  
667
- 668 [4] Zhu, J.-X., Yu, Z.-Q., Yin, Y., Grace, J. R., Issangya A., Cocurrent downflow circulating fluidized  
669 bed (downer) reactors – A state of the art review. The Can. J. of Chem Eng. (1995), Vol 73, Issue5,  
670 662-677.  
671
- 672 [5] Muktar Bashir, Yu, X., Hassan, M., Yassir Makkawi, Modelling and performance analysis of  
673 biomass fast pyrolysis in a solar-thermal reactor, ACS Sustainable Chem. Eng. (2017), 3795–3807.  
674
- 675 [6] Elewuwa, F., Makkawi, Y., A computational model of hydrogen production by steam reforming of  
676 DME in a large-scale CFB reactor: Part II: Parametric analysis, International Journal of hydrogen  
677 production (2016), 19819-19828.  
678
- 679 [7] Yu, X., Hassan, M., Ocone, R., Makkawi, Y., A CFD study of gas-solid separation in a downer  
680 pyrolysis reactor equipped with a novel gas-solid separator- II: Thermochemical performance and  
681 products, Fuel Processing Technology (2015), 51-63.  
682
- 683 [8] Hassan, M and Makkawi, Y., A hydrodynamic model for biomass gasification in a circulating  
684 fluidized bed riser, Chemical Engineering and Processing- Process Intensification, Chemical  
685 Engineering & Processing: Process Intensification (2018), 148–161.  
686
- 687 [9] Bridgwater, A. V., Renewable fuels and chemicals by thermal processing of biomass. Chem. Eng.  
688 J. (2003), 91, 87–102.  
689
- 690 [10] Lin F., Waters C. L., Mallinson R. G., Lobban L. L., Bartley L. E., Relationships between biomass  
691 composition and liquid products formed via pyrolysis. Front. Energy Res. (2015), 3:45  
692

- 693 [11] Yu, Q., et al., *Temperature impact on the formation of tar from biomass pyrolysis in a*  
694 *free-fall reactor*. Journal of Analytical and Applied Pyrolysis (1997), 40-41, 481-489.  
695
- 696 [12] Westerhof, R. J., Brilman, D. W., van Swaaij, W. P., Kersten, S. R., Effect of temperature in  
697 fluidized bed fast pyrolysis of biomass: oil quality assessment in test units, Industrial & Engineering  
698 Chemistry Research (2009), 49, 1160-1168.  
699
- 700 [13] Gerçel, H. F., The production and evaluation of bio-oils from the pyrolysis of sunflower-oil  
701 cake, Biomass and Bioenergy (2002), 23, 307-314  
702
- 703 [14] Gable, Preston, The effect of process variables on pyrolysis in a freefall reactor. Graduate Theses  
704 and Dissertations (2014).  
705
- 706 [15] Ellens, C. J., Design, optimization and evaluation of a free-fall biomass fast pyrolysis reactor and  
707 its products, Graduate Theses and Dissertations, Iowa State University (2009).  
708
- 709 [16] Onay O. and Koçkar O. M., Pyrolysis of rapeseed in a free fall reactor for production of bio-oil,  
710 Fuel (2006), 85, 1921-1928.  
711
- 712 [17] Shen, J. Wang, X.-S., Garcia-Perez, M., Mourant, D., Rhodes M. J., Li, C.-Z., Effects of particle  
713 size on the fast pyrolysis of oil mallee woody biomass, Fuel (2009), 88, 1810-1817.  
714
- 715 [18] Liu, R., Shen, C., Wang, J., Liu, S., Effect of Particle Size of Corn Stalk Fast Pyrolysis on  
716 Physicochemical Properties of Bio-Oil, Journal of Biobased Materials and Bioenergy (2010), 4, 391-  
717 396.  
718
- 719 [19] Uzun, B. B., Pütün, A. E., Pütün, E., Rapid pyrolysis of olive residue. 1. Effect of heat and mass  
720 transfer limitations on product yields and bio-oil compositions, Energy & fuels (2007), 21, 1768-1776.  
721
- 722 [20] Jahirul, M. J., Rasul, M. G., Chowdhury, A. A., Ashwath, N., Biofuels production through biomass  
723 pyrolysis- a technological review, Energies (2012), 5, 4952-5001.  
724
- 725 [21] Huard, M., An Investigation of a Novel Gas–Solid Separator for Downer Reactors, M. E. Sc. Thesis  
726 The University of Western Ontario, London, Canada (2009).  
727

- 728 [22] Huard, M., Berruti, F., Briens, C., Experimental Study of a Novel Fast Gas-Solid Separator for  
729 Pyrolysis Reactors, *International Journal of Chemical Reactor Engineering* (2010), 8, 1542-6580.  
730
- 731 [23] Boateng, A. and Mtui, P., CFD modeling of space-time evolution of fast pyrolysis products in a  
732 bench-scale fluidized-bed reactor, *Applied Thermal Engineering* (2012), 33, 190-198.  
733
- 734 [24] Pasangulapati, V., Devolatilization characteristics of cellulose, hemicellulose, lignin and the  
735 selected biomass during thermochemical gasification: experiment and modeling studies. Thesis,  
736 Oklahoma State University (2012).  
737
- 738 [25] Boateng, A. A.; Daugaard, D. E.; Goldberg, N. M.; Hicks, K. B. Bench-scale fluidized-bed  
739 pyrolysis of switchgrass for bio-oil production. *Ind. Eng. Chem. Res.* 2007, 46 (7), 1891–1897.  
740
- 741 [26] ANSYS Fluent. *Ansys fluent theory guide*, version 15.0; Ansys Inc.: Cecil Township, PA.  
742
- 743 [27] Vasquez, S. A. and Ivanov, V. A. “A Phase Coupled Method for Solving Multiphase  
744 Problem on Unstructured Meshes,” *Fluids Engineering Division Summer Meeting, ASME*,  
745 Boston, 11-15 June 2000.  
746
- 747 [28] Demirbas, Ayhan, *Production and Characterization of Bio-Chars from Biomass via Pyrolysis*,  
748 *Energy Sources, Part A: Recovery, Utilization, and Environmental Effects*, Volume 28 (2006) - Issue 5  
749
- 750 [29] Seebauer, V., Petek, J., Staudinger, G. Effects of particle size, heating rate and pressure  
751 on measurement of pyrolysis kinetics by thermogravimetric analysis Author links open overlay  
752 panel, *Fuel* (1997), Volume 76, Issue 13, 1277-1282.  
753
- 754 [30] Septien, S., Valin, S., Dupont, C., Peyrot, M., Salvador, S., Effect of particle size and  
755 temperature on woody biomass fast pyrolysis at high temperature (1000-1400 degrees C). *Fuel*  
756 (2012), 97, 202-210.  
757
- 758 [31] Makkawi, Y. and Wright, P. C., The void function and effective drag force for fluidized  
759 beds. *Chemical Engineering Science* (2003), 58 (13), 2035-2051.  
760
- 761 [32] Ghirelli, F., Hermansson, S., Thunman, H., Leckner, B., Reactor residence time analysis  
762 with CFD, *Progress in Computational Fluid Dynamics*, (2006), 6 (4/5), 241–247.

763

764 [33] A.V. Bridgwater, G.V.C. Peacocke, Fast pyrolysis processes for biomass, Renewable &  
765 Sustainable Energy Reviews (2000), 4, 1–73.

ACCEPTED MANUSCRIPT

**Highlights**

- Parametric analysis of fast pyrolysis in a downer reactor has been carried out using CFD modeling.
- The pyrolysis temperature is the most effective parameter in the bio-oil yield.
- The size of the heat carrier (sand) affects the hydrodynamics and overall thermochemical conversion.
- The nitrogen flow rate strongly affects the gas residence time and devolatilization rate.